Numerical Analysis on Reusable Rocket Aerodynamics with Reduced-Yaw-Force Configurations

By Ayano INATOMI, [1] Keiichi KITAMURA, [1] and Satoshi NONAKA[2]

[1] *Yokohama National University, Yokohama, Japan*
[2] *Institute of Space and Astronautical Science, JAXA, Sagamihara, Japan*

(Received June 30th, 2017)

It is known that aerodynamic characteristics of a slender body vary substantially at high angles-of-attack (AoAs), and then, will have strong impacts on its flight. For, example, the yaw force makes flight unstable. In this study, we investigated the relation between the yaw force and the configuration, and details of flowfield around the slender-bodied-vehicle numerically. The configuration consisting of "nose cone" and "square aftbody" parts was employed as the baseline, and then, compared with other three configurations having different fineness ratios. According to our computed results, in the case of 50 degrees of AoA, the longer the model became, the more asymmetry appeared: yaw force and asymmetry were found to be attributed not only to the length of the body, but also to the nose bluntness. On the contrary, in the case of 140 degrees, the shorter the model became, the more asymmetry appeared. Furthermore, the large nose bluntness increased C_Y. Interestingly, this trend is totally opposite to that observed at 50 degrees. It had been considered that the large nose bluntness and the small fineness ratio can reduce asymmetry and C_Y, however, this study showed that it is not true in the case over 90 degrees, due to complex wake flow structure discovered in the present numerical simulations.

Key Words: Aerodynamic Characteristics, CFD, Reusable Rocket, Yaw Force, Asymmetric Vortices

Nomenclature

C_Y	:	yaw force coefficient
F	:	force
L	:	reference length (length of model)
L_{base}	:	width of base
p	:	static pressure
q	:	dynamic pressure
S	:	reference area (base)
V	:	freestream velocity
α	:	angle of attack
ρ	:	density

Subscripts

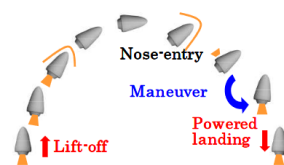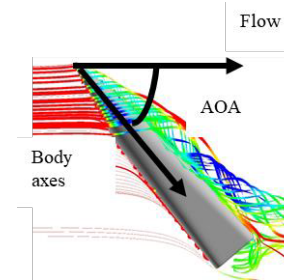|		
x, y, z	:	x, y, or z direction

Fig. 1. nose entry.[2]

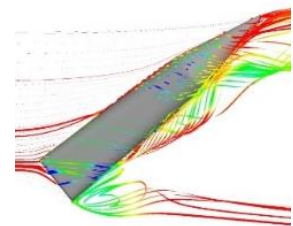
Fig. 2. RVT.[3]


Fig. 3. Definition of angle of attack.

Fig. 4. Separated flow.

1. Introduction

A reusable rocket can be used several times and is expected to reduce its space transportation cost. [1] Vertical take-off and vertical landing[2] (Fig. 1.) is one of system concepts for reusable rockets. The representative reusable rocket is RVT (Reusable Vehicle Testing)[3] in JAXA (Fig. 2.). Such vehicles should have slender configurations to achieve appropriate aerodynamics for its flight.

It is known that aerodynamic characteristics of such a slender body varies substantially at high angles-of-attack (AoAs) (Fig. 3.), in which, flowfields become asymmetry because of large separations (Fig. 4.), producing yaw force. [4,5] A large yaw force will destabilize the flight. In fact, an earlier study on a particular configuration[4] reported large C_Y (yaw force coefficient) and high flow asymmetry at high AoAs (50 degrees or more).
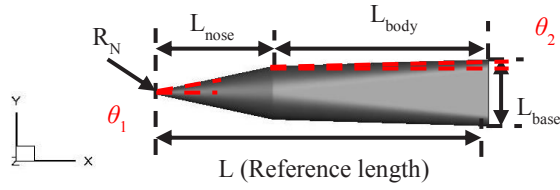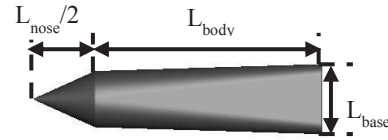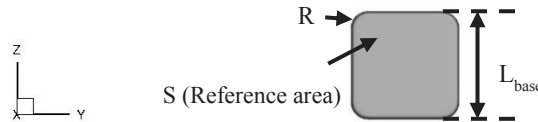
(a) Model A (baseline)
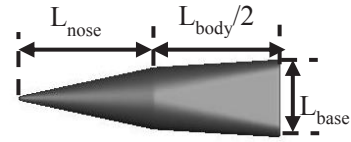
(c) Model C (half "body" length)
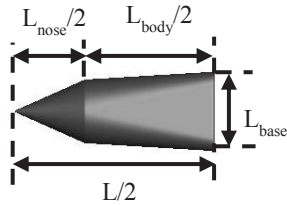
(b) Model B (half total length)

(d) Model D (half "nose" length)

(e) Base view of Model A and B

Fig. 5.   Configurations.

Table 1.   Scale of the computational configurations.

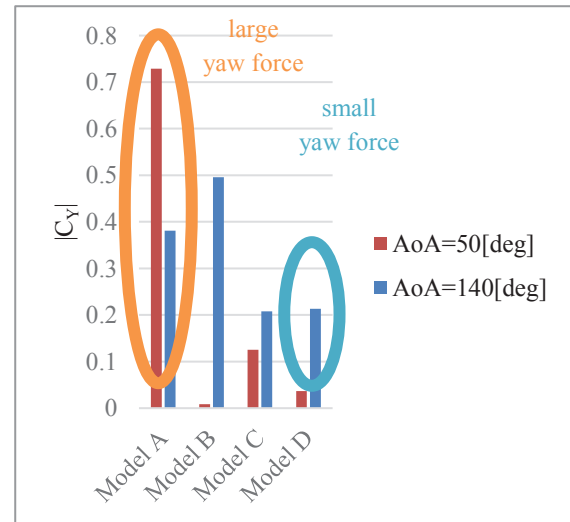| model	(a)Model A	(b)Model B
L[mm]	307.02	**153.51**
L_{nose}[mm]	106.84	**53.42**
L_{body}[mm]	200.18	**100.09**
L_{base}[mm]	62.1	62.1
projected area S[mm²]	3770.57	3770.57
R_N[mm]	2.25	**1.125**
R[mm]	10	10
diameter of nose[mm]	49.86	49.86
θ_1[degree]	12.21	**24.38**
θ_2[degree]	1.77	**3.53**

Fig. 6.   Yaw force coefficients.

As the first step of our study covering whole the flight envelop (and hence, all the possible angles of attack) of a reusable rocket, here we selected the 50 and 140 degrees (corresponding to 40 deg. if seen from the vehicle base) for particular reasons. Typically, the flowfields around flight vehicles are known to be either 1) symmetry and steady (at small angles), 2) asymmetry and steady (at moderate or high angles), or 3) asymmetry and unsteady (at very high angles,

such as 90 deg). Among still not-yet-fully-understood flow physics in 2) and 3), we will pay a special attention to 2) because of cheaper computational cost required.

In the earlier study using RANS (Reynolds-Averaged-Navier-Stokes), it was discovered that the flowfield around a slender configuration was clearly asymmetry, yet steady, at 50 and 140 degrees, whereas asymmetry and "unsteady" around 90 degrees, in which more sophisticated unsteady simulations

such as LES (Large Eddy Simulation) would be necessary. Furthermore, the flowfields have not been fully explained or even studied at over 90 degrees (e.g., 140 degrees). These are the reasons why we focused on both the 50 and 140 AoAs in our present, RANS simulation study.

In addition, it is known that configurations such as fineness ratio and a half-apex-angle affect a yaw force. [5] Specifically, the blunt nose can reduce asymmetry.[5] Besides, the early studies[6,7] show that the structure of the vortices around the body at high angle of attack. However, the detailed links between the flow asymmetry, C_Y, and the vehicle configurations particularly at more than 90 degrees of AoA have not been fully explained yet. We will numerically investigate the above-mentioned relations in this work.

2. Analysis Configurations

Figure 5 shows the all configurations which we investigated. In addition, the yaw force coefficients are shown in Fig. 6. The C_Y of the Model C is larger in 140 AoAs than 50 AoAs, like the Model B and the Model D. The Model D can reduce C_Y most, however, the reason was unclear why the C_Y becomes small. We want to know the mechanism of the yaw force getting large. Therefore, we focused on the Model A and Model B especially, which indicated large yaw force coefficients here.

We use the configuration consisting of "nose cone" and "square body" parts ("Model A") as the baseline (Fig. 5 (a)),[4,8] and, Model B, which has different fineness ratio from that of Model A, proposed as in Fig. 5 (b). Model C has a half body length of Model A and Model D has a half nose length of Model A (Fig. 5 (c), (d)). In various configurations used in the early studies,[9,10] Model A is a promising candidate for reusable rockets because its separation point is rather fixed due to the square portion. In the earlier study, it is known that the squared body can reduce asymmetry of the flowfield than the cylinder body. [8] Moreover, it is also known that the face receiving the aerodynamic force is increased, and the lift force is generated by making the cross-sectional shape not a circle but a square.[11] In Fig. 5 (a), R_N is the radius of nose tip, L_{nose} is the nose-cone part length and L_{body} is the square-body part length. θ_1, θ_2 are the half apex angles of the nose and the body, respectively. In addition, S is the reference area as shown in Fig. 5 (e). It is determined as follow.

$$S = (L_{base} - 2R)^2 + \pi R^2 + 4R(L_{base} - 2R) \qquad (2)$$

We investigated three different configurations based on Model A, however, in this paper, we focus only on two of these configurations which showed great yaw force. The size of Model A and Model B are shown in Table 1. Model B has half X-directional length of Model A. In Table 1., boldfaced types and gray backgrounds indicate that the parameters are different from Model A.

For instance, the half apex angle of the nose of Model B ($\theta_1 = 24.38$[deg]) is larger (almost twice) than that of Model A ($\theta_1 = 12.21$[deg]). Moreover, θ_2 of Model A ($\theta_2 = $

1.77[deg]) is smaller (almost half) than that of Model B ($\theta_2 = 3.53$[deg]).

3. Numerical Setup

3.1. Governing equation

Governing equations are Navier-Stokes equations.

$$\frac{\partial Q}{\partial t} + \frac{\partial F_{e_k}(Q)}{\partial x_k} = \frac{1}{Re} \frac{\partial F_{v_k}}{\partial x_k} \qquad (1)$$

Q is a conservative variables, F_e is inviscid variables, F_v is viscous variables. These are as follows.

$$Q = \begin{pmatrix} \rho \\ \rho u_l \\ e \end{pmatrix}, \quad F_e(Q) = \begin{pmatrix} \rho u_k \\ \rho u_l + p\delta_{lk} \\ (e+p)u_k \end{pmatrix}$$

$$F_v(Q) = \begin{pmatrix} 0 \\ \tau_{lk} \\ u_m \tau_{mk} + \frac{\kappa}{(\gamma-1)Pr} \frac{\partial T}{\partial x_k} \end{pmatrix} \qquad (2)$$

Where subscripts k, l and m take 1, 2, 3 denoting the Cartesian coordinates. Then, ρ, e, p, u_i, τ_{ij}, κ, T, γ, Re, Pr and δ_{ij} are density, total energy per unit volume, pressure, velocity vector, stress tensor, coefficient of heat conduction, temperature, heat capacity ratio, Reynolds number, Prandtl number, and Kronecker delta, respectively. These have already been non-dimensionalized by

$$\rho = \frac{\tilde{\rho}}{\rho_\infty}, e = \frac{\tilde{e}}{\rho_\infty a_\infty^2}, p = \frac{\tilde{p}}{\rho_\infty a_\infty^2}, u_i = \frac{\tilde{u}_i}{a_\infty},$$

$$\kappa = \frac{\kappa}{\kappa_\infty}, T = \frac{\tilde{T}}{T_\infty}, Re = \frac{\rho_\infty a_\infty L}{\mu_\infty} = \frac{Re_\infty}{M_\infty}, Pr = \frac{c_p \mu_\infty}{\kappa_\infty} \qquad (3)$$

where tildes ($\sim$) and infinity (∞) indicate dimensional quantities and freestream values, respectively. L is the reference length, and a_∞ is the freestream sound speed. Moreover, μ_∞ is the freestream viscosity coefficient and C_P is the specific heat at constant pressure.

3.2. Numerical methods

In this study, we employ CFD solver "FaSTAR"[12] developed at JAXA. All calculations are unsteady calculations. The time integration method is preconditioned LU-SGS along with dual-time-stepping and backward difference (second order), [13] and reconstruction method is GLSQ (second order). [14] The turbulence model is Spalart-Allmaras (SA) RANS model,[15] which is one of popular RANS turbulence models in aerospace engineering.

Note that more sophisticated turbulence models such as SST (Shear-Stress-Transport)[16] or DDES (Delayed-Detached-Eddy-Simulation)[17] would enhance the solution resolution, in expense of computational cost. The SA model, on the other hand, is in fact a good compromise between its accuracy and efficiency, particularly for the flow physics of our interest: The earlier study[4,18] on the similar configurations resulted in the

similar solutions (C_Y and the flowfield) between SA and DDES models, as long as steady flowfields are obtained at low or moderate AoAs (typically 50 degrees or less).

Moreover, we employ Venkatakrishnan limiter as the slope limiter. We run calculations on supercomputer "JSS2" in JAXA.

3.3. Computational grids

We employ "HexaGrid"[19] developed at JAXA. HexaGrid is a software which automatically generates grids based on hexahedron from STL data. Figure 7 shows the grid around the body. Outer boundary is set to 25L away from the body. The origin is the nose tip, the body axis direction is the X axis and the direction which determines the yaw force is the Y axis. The Z axis is defined so that it is orthogonal to those two.

Furthermore, we use refinement boxes for arranging fine grids only in the region where vortices are formed (Fig. 8). Since the large vortices are known to the base at 50 degrees and near the nose at 140 degrees of AoA, according to our preliminary computations, we prepared large refinement boxes in these parts.

We decided the number of cells as in Table 2. We generated grids so that the first cell height almost satisfies $y^+<1$.
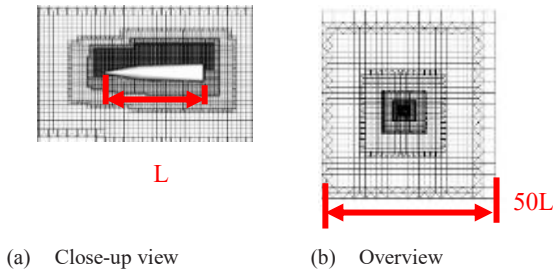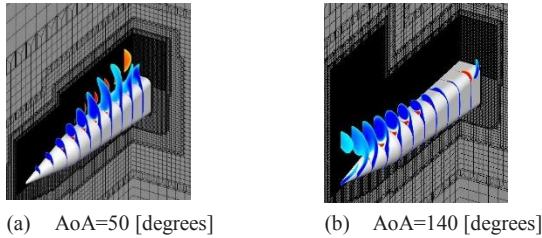

| (a) Close-up view | (b) Overview |

Fig. 7. Computational grid.

| (a) AoA=50 [degrees] | (b) AoA=140 [degrees] |

Fig. 8. Grid refinement and X Vorticity.

Table 2. Number of grids.

model	(a)Model A		(b)Model B	
AoA[deg]	50	140	50	140
No. of cells	1.75M	8.95M	4.01M	5.44M
y^+	0.78	0.81	1.0	0.84

3.4. Numerical conditions

The Mach number is 0.086 (flow speed is 30[m/s]), the freestream Reynolds number is set to 6.02×10^5. Moreover, the reference length is 0.307[m], the static pressure is set to 99920[Pa], and the static temperature is 291.15[K]. These conditions are the same as that of wind tunnel test.[8] In this study, we defined the gravity center where 65% of total length from the nose tip.

3.5. Definition of yaw force coefficient

The yaw force coefficient is defined as follows.

$$C_Y = \frac{F_y}{\frac{1}{2}\rho_\infty U_\infty^2 S} \tag{4}$$

Where U_∞, S, and F_y are the freestream velocity, the reference area (Base area), and the yaw force, respectively (Fig. 9).
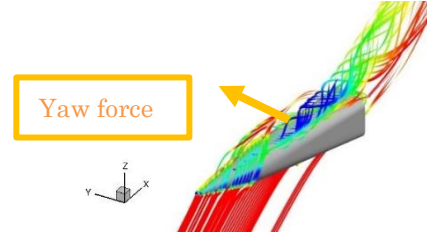

Fig. 9. Direction of Yaw force.

4. Results and discussion

4.1. Yaw force

We obtain yaw force coefficients and visualized flowfields for two configurations (Model A and Model B) at 50 and 140 degrees of AoA.

From the yaw force coefficients in Table 3., the value is smallest in the cases of Model B at 50 degrees followed by Model A at 140 degrees of AoA.

Table 3. C_Y.

model	(a)Model A		(b)Model B	
AoA[deg]	50	140	50	140
C_Y	0.729	0.381	8.36×10^{-3}	0.496
Sym/ Asym	Asym	Asym	Sym	Asym

Figures 10 and 11 indicate the visualization results of each case. The top figures show the on-surface pressure coefficient (viewed from +z), and the bottom figures are the X vorticity. From these results, it can be said that the flowfield appears symmetric in the case of Model B at 50 degrees. On the contrary, apparent asymmetry can be observed in the cases of Model A at 50 degrees and Model B at 140 degrees of AoA. Therefore, the opposite trend appears between 50 degrees and 140 degrees of AoA. Now that we have observed a relation between the configurations and the yaw forces, in the next section, we will explain the difference of flowfields around the body between 50 degrees and 140 degrees of AoA.
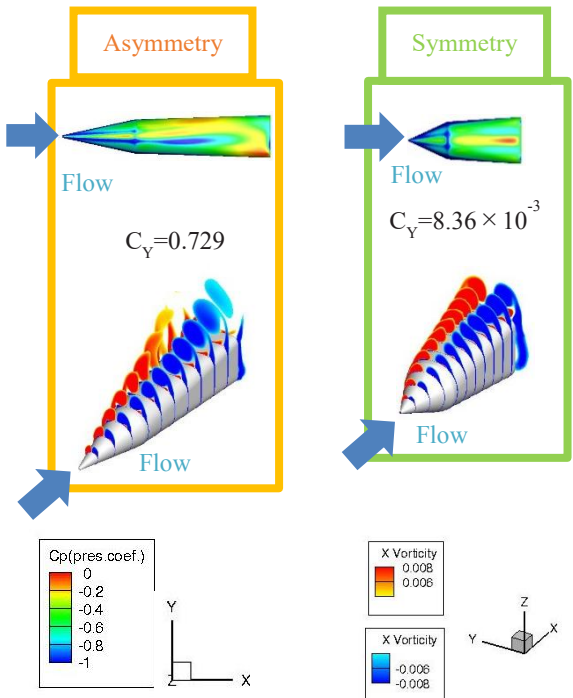
4.2. Relation between yaw force and flow field

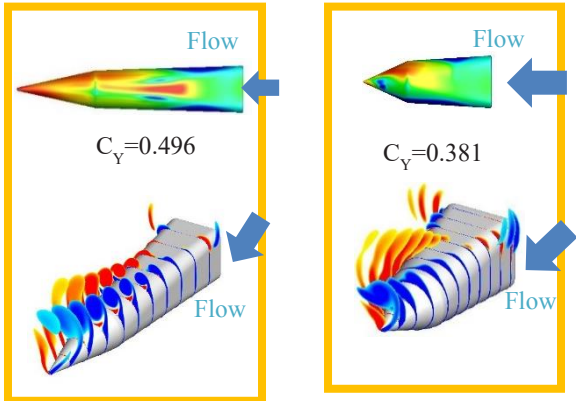#### 4.2.1 AoA = 50 [degrees]

A. Model A (Baseline)

In Fig. 12, the black lines indicate the streamlines around the body. From this figure, we can observe the evolution of the

longitudinal vortices in the leeward side of the body. Furthermore, Fig. 13 shows C_P and the streamlines on the body surface seen from the +Z direction.

(a) Model A   (b) Model B

Fig. 10.   Summery (AoA = 50 [degrees]).

(a) Model A   (b) Model B

Fig. 11.   Summery (AoA = 140 [degrees]).

From Fig. 13, the flowfield is symmetry on the section of 10% of the total length from the nose tip, whereas asymmetry appears on the section of 70% and 90%. In order to confirm to these, we show in Fig. 14 velocity vectors on the section of 10%, 70% and 90% of total length. These vectors are colored with X vorticity. From Fig. 14 (a), two symmetric vortices (V1, V2) are generated at the nose (10%). However, the right vortex (V2) exists and the left vortex structure (V1) collapses near the gravity center (70%) as evident in Fig. 14 (b). In addition, V2 on the 90% section has grown from the 70 % section in Fig. 14 (c). These results illustrate that the flowfield is symmetry on the 10% section but asymmetry on the 70% and 90% sections.

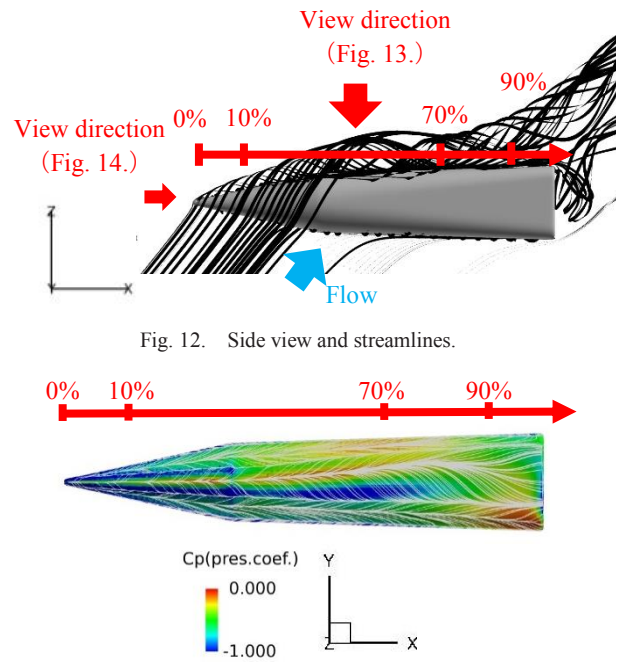From these results, we can say that the vortex became

Fig. 12.   Side view and streamlines.

Fig. 13. C_P and surface streamline (top view).

(a)   X = 10 %
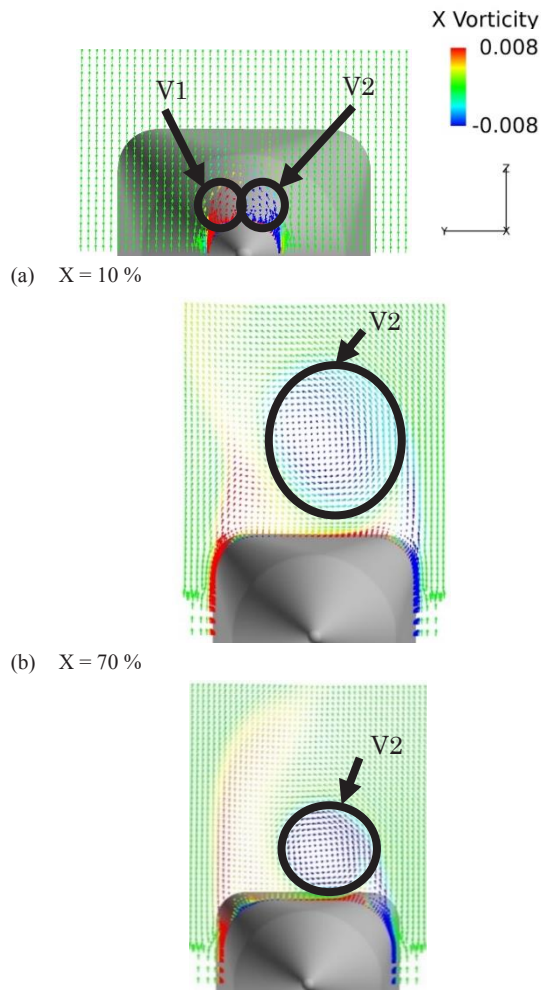

(b)   X = 70 %

(c)   X = 90 %

Fig. 14.   Velocity vectors with X Vorticity.

asymmetry in the downstream, and this caused the asymmetric C_P distribution (Fig. 13).

As a result, the large yaw force (C_Y=0.729) was generated.

B. Model B (Half Length)

The flowfield appears totally symmetry in Fig. 15 which is confirmed from the on-surface C_P distribution along with surface streamlines (in white) seen from the +Z direction. Since the flowfields are symmetry on all, we show only the 70% section as the representative of these planes in Fig. 16, in which symmetry vortices (V1, V2) are observed. This is why yaw force (C_Y=8.36×10^{-3}) is negligibly small in this case.
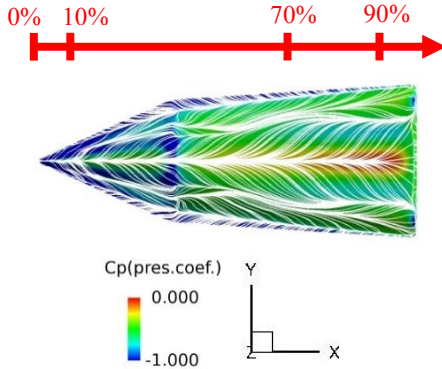
Fig. 15. C_P and surface streamline (top view).
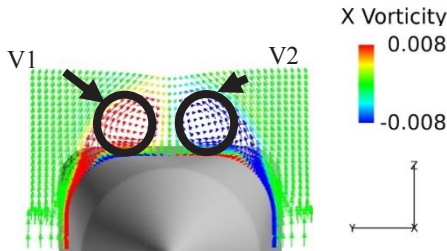
Fig. 16.   Velocity vectors with X Vorticity (X = 70%).

C. Summary of AoA = 50 [degrees]

As we mentioned above, the flowfield of Model A becomes asymmetry clearly, although that of Model B is symmetry. This results in the larger C_Y of Model A compared to Model B. As we mentioned in Section 2, Model B has a larger half apex angle from Model A, and the length of Model B is half of Model A. Thus, we can say that the configuration having a short nose and a large half apex angle would reduce yaw force. An earlier study[4] on similar configurations also reported that the blunt nose can suppress asymmetry. In other words, our result is consistent with the literature for this AoA.

4.2.2   AoA = 140 [degrees]

A. Model A (Baseline)

To the best of the authors' knowledge there is no prior work which examined detailed aerodynamics at this AoA. Figure 17. indicates streamlines in which we can see vortices. Figure 18. shows the on-surface streamlines and C_P distribution. C_P in the downstream 70% and higher is totally symmetry as seen from this figure. We have focused on the three sections from the upstream to the downstream in the previous sections. In 140 degrees of AoA, however, we omit section of 10% because vortex does not exist. As shown in Fig. 19 (a), two asymmetric

vortices (V3, V4) can be seen on the 70% section. These vortices are constituted of the flows which passed through the base (Fig. 17), and thus, these are different from the two vortices (V1, V2) which are generated at nose tip in 50 degrees of AoA. On the 90% section, the vortex structure (V3) collapses while the vortex (V4) is further developed, compared to the 70% section. Therefore, inspite of the different generation mechanisms of vortices, asymmetry can be seen in the downstream at this 140 deg. AoA, as in the case of 50 degrees. For this reason, the yaw force (C_Y = 0.381) is generated, which is smaller than C_Y=0.729 at 50 deg., but still significant.

B. Model B (Half Length)

Visualized results are displayed in Figs. 20 - 22 as in the other cases. Asymmetry can be seen clearly in Fig. 21. Furthermore, the small asymmetry vortices (V3, V4) are produced near the body as evident in Fig. 22 (a). In Fig. 22 (b), only V4 exists whereas V3 already decayed. As a result, the C_P distribution becomes asymmetry from the vicinity of the gravity center (65%) to the nose (70% and 90%) (Fig. 21). These results can be also confirmed from the development of the large yaw force (C_Y=0.496).

Now, we discuss the reason why the flowfield is asymmetry clearly at the nose. The swirling flows appear in three places, the upstream and the downstream (Fig. 19, Fig. 22, V3, 4), and the flow especially gathers in the forward (downstream) of the body. From this fact and the visualization result, we can say that the nose blunt body which is rear-positioned when $\alpha >$ 90° raises asymmetry of the flowfield. Let us briefly explain the reason of the asymmetric vortices by using Fig. 23. Figure 23 shows the relation between nose bluntness and asymmetry. In this figure, nose-sharp configuration (Model A) (i.e., sharp "trailing edge" when $\alpha > 90°$) and a nose-blunt configuration (Model B) (i.e., blunt "trailing edge" when $\alpha > 90°$) are illustrated. It is known that fluids tend to flow along a sharp trailing edge, whereas they can separate more easily and become asymmetry in the case of a blunt trailing edge, such as Karman vortices. In summary, we consider the reason of asymmetric flowfields of the Model B is that the "nose cone" part (i.e., downstream part if AoA > 90°) behaves as a blunt "trailing edge" in this study.

C. Summary of AoA = 140 [degrees]

C_Y of Model B (C_Y=0.496) is larger than that of Model A (C_Y=0.381). Thus, we have obtained the opposite results from those of 50 degrees. That is, Model B generates the more asymmetric flowfield at 140 degrees than that at 50 degrees, whereas the flowfield is symmetry at 50 degrees. Moreover, the flowfields are asymmetry around both configurations at 140 degrees. In other words, asymmetry can occur easily over 90 degrees. The reason is that the blunt trailing edge makes vortex asymmetry in downstream.

Moreover, C_Y of the Model C in 140 AoAs is as large as the Model D. From this result, the bluntness of body part also effects asymmetry and yaw force. The Model B and the Model C have blunt bodies and this is one of the reason of asymmetry.
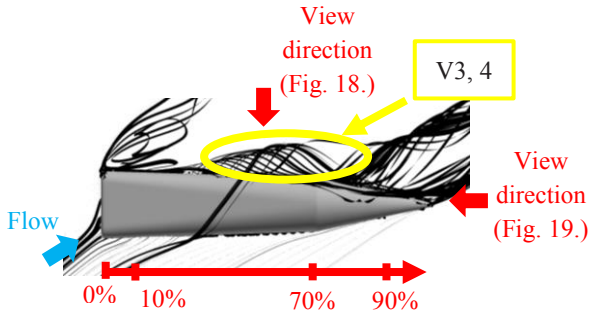
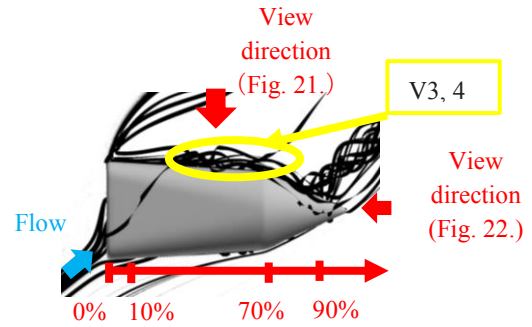Fig. 17.   Side view and streamlines (Model A).

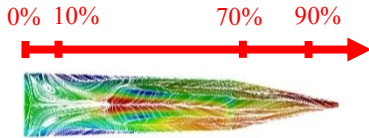Fig. 20.   Side view and streamlines (Model B).

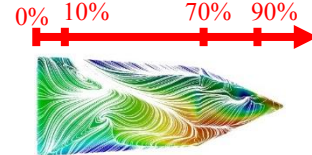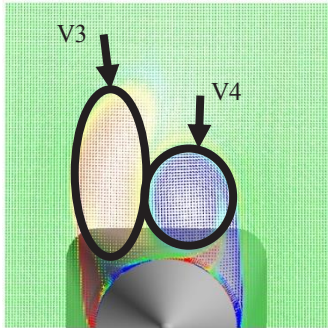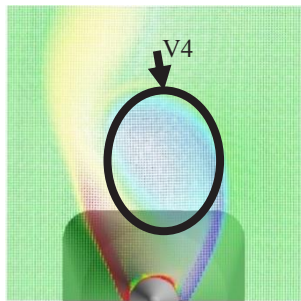Fig. 18. C_P and surface streamline (top view of Model A).
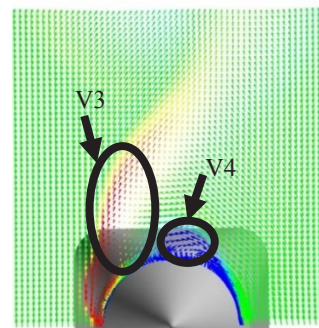

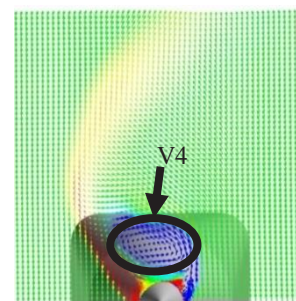Fig. 21. C_P and surface streamline (top view of Model B).

(a)   X = 70%

(a) X = 70%

(b)   X = 90%

Fig. 19.   Velocity vectors with X Vorticity (Model A).

(b) X = 90%

Fig. 22.   Velocity vectors with X Vorticity (Model B).

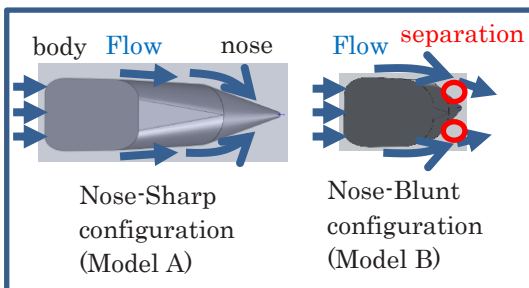
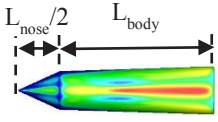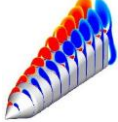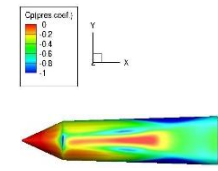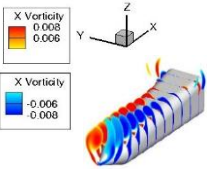Fig. 23.   Nose-Bluntness and asymmetry (when $\alpha > 90°$).

5.   Conclusions

In this study, we numerically investigated the details of flowfields around potential reusable rocket configurations at high angles-of-attack. Then, we obtained the results as follows by comparing different configurations.

- At 50 degrees, the longer the body becomes, the more asymmetry of two vortices is developed. From this result, we confirm that the blunt configuration having the short total length reduces asymmetry.

- At 140 degrees, the configuration which has the short total length increases asymmetry; this is the opposite trend to that at 50 degrees. This is because flowfields increase asymmetry while passing along the blunt nose (i.e., rear part when $\alpha > 90°$). Moreover, the blunt body is also one of the reason of asymmetry.

Considering these results, we explain why the Model D best suppressed the asymmetry. The Model D has a half-length of the nose part and the same length of the body part as the model A (baseline). The half long nose reduced asymmetry at 50 AoA, whereas the long body kept symmetry at 140 AoA (Table 4.).

Table 4. Results of the Model D.

AoA [deg]	Pressure coefficient	X Vorticity
50		
140		

We conclude from these results as follows: It is newly discovered that blunt configurations which have small fineness ratios likely to show asymmetry over 90 degrees.

We have selected the present Reynolds number from the wind test in the similar work (in which the flow simulation and the experiment matches well each other).[8] It is already reported, however, that the Reynolds number can significantly affect C_Y and the asymmetry of the flowfield, particularly at turbulent transition (as in this work).[20] Thus, we would like to simulate the flowfields at different Reynolds numbers (e.g., flight Reynolds number) in the future. Such a work on Reynolds effects is deferred to the future work.

Acknowledgments

References

1) Kawado, H., Ishikawa, K., Niu, K., Takida, J., Obase, K., and Fukuda, Y.: Status of Research and Development Activities on Reusable Launch Vehicle, Technical Report of Mitsubishi Heavy Industries, **51**, No.4, 2014, https://www.mhi.co.jp/technology/review/pdf/514/514044.pdf (accessed February 8, 2017) (in Japanese).

2) Kei, K., Takagi, R., Oyama, S., Fujii, T., and Yamamoto, S.: Computational Analysis of Aerodynamic Characteristics during the Launch and Return of the Reusable Observation Vehicle, 23rd Symposium on Computational Fluid Dynamics, 2009 (in Japanese).

3) About the third reusable rocket experiment machine taking off and landing experiment (RVT-9) in JAXA, http://www.jaxa.jp/press/2003/11/20031112_rvt_j.html (January 7, 2017) (in Japanese).

4) Aogaki, T., Kitamura, K., and Nonaka, S.: Computational Study of Aerodynamic Characteristics of Reusable Rocket at High-Angle-of-Attack, AIAA Paper 2017-1212, 2017.

5) Ericsson, L. E. and Reding, J. P.: Steady and Unsteady Vortex-Induced Asymmetric Loads on Slender Vehicles, *AIAA J.*, **18** (1981),pp.97-109.

6) Jia, M., Watanuki, T., and Kubota, H.: The Visualization of Separated Flow Over Slender Bodies at High Angle of Attack, *Transactions of the Visualization Society of Japan*, **14** (1994), pp.37-46, (in Japanese).

7) Cummings, R., Forsythe, J., Morton, S., and Squires, K.: Computational Challenges in High Angle of Attack Flow Prediction, *Progress in Aerospace Science*, **39**, (2003), pp.369-384.

8) Kinami, T.: Aerodynamic Characteristics of Slender Bodies at Turnover, graduation thesis, Yokohama National University, Kanagawa, Japan, 2016, (in Japanese).

9) Fujimoto, K.: Computational Aerodynamic Analysis of Capsule Configurations Toward the Development of Reusable Rockets, *Journal of Spacecraft and Rockets*, **43** (2006), pp.77-83.

10) Imamura, Y.: Attitude Maneuver of VTOL Rocket in Landing Phase, master's thesis, Tokyo University, Tokyo, Japan, 2008.

11) Nakamura, M., Nonaka, S., and Inatani, Y.: Aerodynamics of Reusable VTOL Rocket in Return Flight, Proceedings of 58th Space Sciences and Technology Conference, 2014 (in Japanese).

12) Hashimoto, A., Murakami, K., Aoyama, T., Ishiko, K., Hishida, M., Sakashita, M., and Lahur, P.: Toward the Fastest Unstructured CFD Code "FaSTAR", AIAA Paper 2012-1075, 2012.

13) Kitamura, K., Shima, E., Fujimoto, K., and Wang, Z. J.: Performance of Low-Dissipation Euler Fluxes and Preconditioned LU-SGS at Low Speeds, *Commun. Comput. Phys.*, **10** (2011), pp. 90-119.

14) Shima, E., Kitamura, K., and Haga, T.: Green-Gauss/Weighted-Least-Squares Hybrid Gradient Reconstruction for Arbitrary Polyhedra Unstructured Grids, *AIAA J.*, **51** (2013), pp.2740-2747.

15) Spalart, P. and Allmaras, S.: A One-Equation Turbulence Model for Aerodynamics Flows, AIAA Paper 1992-439, 1992.

16) Menter, F. R.: Two-Equation Eddy-Viscosity Turbulence Models for Engineering Applications, *AIAA J.*, **32** (1994), pp. 1598-1605.

17) Spalart, P. R., Deck, S., Shur, M. L., Squires, K. D., Strelets, M. K., and Travin, A.: A New Version of Detached-Eddy Simulation, Resistant to Ambiguous Grid Densities, *Theoretical and Computational Fluid Dynamics*, **20** (2006), pp. 181–195.

18) Aogaki, T., Kitamura, K., and Nonaka, S.: Numerical Analysis of Aerodynamic Characteristics of Reusable Rocket at High-Angle-of-Attack, 48th ANSS, Kanazawa, Japan, 2016 (in Japanese).

19) Hashimoto, A., Murakami, K.., Aoyama, T., Yamamoto, K., and Murayama, M.: Drag Prediction on NASA CRM Using Automatic Hexahedra Grid Generation Method, *Journal of Aircraft*, **51** (2014), pp.1244-1267.

20) Kubota, H., Arai, I., and Matsuzawa, M.: Flat Spin of Slender Bodies at High Angles of Attack, *Journal of Spacecraft*, **20** (1983), pp.108-114.